Research Article

Nano Research
2020, 13(11): 3142–3150

ISSN 1998-0124 CN 11-5974/O4
https://doi.org/10.1007/s12274-020-2985-4

Self-assembly of highly ordered DNA origami lattices at solid-liquid interfaces by controlling cation binding and exchange

Yang Xin[1], Salvador Martinez Rivadeneira[1], Guido Grundmeier[1], Mario Castro[2], and Adrian Keller[1] (✉)

[1] *Technical and Macromolecular Chemistry, Paderborn University, Paderborn 33098, Germany*
[2] *Grupo Interdisciplinar de Sistemas Complejos and Instituto de Investigación Tecnológica, Universidad Pontificia Comillas de Madrid, Madrid 28015, Spain*

Received: 9 June 2020 / **Revised:** 11 July 2020 / **Accepted:** 12 July 2020

ABSTRACT

The surface-assisted hierarchical self-assembly of DNA origami lattices represents a versatile and straightforward method for the organization of functional nanoscale objects such as proteins and nanoparticles. Here, we demonstrate that controlling the binding and exchange of different monovalent and divalent cation species at the DNA–mica interface enables the self-assembly of highly ordered DNA origami lattices on mica surfaces. The development of lattice quality and order is quantified by a detailed topological analysis of high-speed atomic force microscopy (HS-AFM) images. We find that lattice formation and quality strongly depend on the monovalent cation species. Na^+ is more effective than Li^+ and K^+ in facilitating the assembly of high-quality DNA origami lattices, because it is replacing the divalent cations at their binding sites in the DNA backbone more efficiently. With regard to divalent cations, Ca^{2+} can be displaced more easily from the backbone phosphates than Mg^{2+} and is thus superior in guiding lattice assembly. By independently adjusting incubation time, DNA origami concentration, and cation species, we thus obtain a highly ordered DNA origami lattice with an unprecedented normalized correlation length of 8.2. Beyond the correlation length, we use computer vision algorithms to compute the time course of different topological observables that, overall, demonstrate that replacing $MgCl_2$ by $CaCl_2$ enables the synthesis of DNA origami lattices with drastically increased lattice order.

KEYWORDS

DNA origami, self-assembly, lattice formation, high-speed atomic force microscopy, topological analysis

1 Introduction

Regular macroscopic structures with controllable nanoscale features are attracting increasing attention in the fields of nanoscience and materials science owing to their remarkable properties [1–5]. DNA molecules are widely used as a building material for the programmable self-assembly of nanostructures and functional molecular devices [6–12]. In particular, the DNA origami technique allows for the high-yield assembly of almost arbitrary nanoscale shapes [13–16]. Surface-assisted hierarchical self-assembly of DNA origami nanostructures offers a simple yet efficient route for scaling up the total structure size, yielding regular DNA origami lattices over large surface areas that can be utilized as molecular lithography masks for the controlled arrangement of various functional species [17, 18]. To arrange individual DNA units into larger assemblies, different intermolecular interactions are employed, for example, sticky-end hybridization and blunt-end stacking [17, 19–22]. Taking advantage of the geometric complementarity of the DNA origami shapes is one of the most attractive approaches [18, 21–24], in which ordered monolayers are achieved by controlling the attractive electrostatic forces between the substrate surface and the DNA origami nanostructures without the need for tailoring specific attractive interactions between the individual DNA origami shapes.

In our previous work, we have investigated the development of ordered DNA origami lattices on mica surfaces in the presence of different concentrations of Na^+ and Mg^{2+} ions [23]. The Na^+ ions compete with Mg^{2+} and can partially replace the adsorbed Mg^{2+} at the mica–DNA interface [20, 21, 25, 26]. Mg^{2+} ions are commonly used to stabilize DNA origami structures by compensating the repulsion of the negative charges of the DNA phosphates [27], and enable DNA structures to adsorb to negatively charged mica surfaces. Since divalent cations are much more effective than monovalent cations in compensating for the negative charges carried by mica surfaces [28–30], the Mg^{2+}–Na^+ ion exchange results in weakened DNA binding and increased surface mobility, which thus leads to enhanced surface diffusion and may even induce DNA origami desorption [23]. Furthermore, the repulsive DNA–DNA interactions are also affected by changes in the Na^+ and Mg^{2+} concentrations. Therefore, by varying the Na^+/Mg^{2+} ratio, the surface behavior of the DNA origami nanostructures, such as adsorption, diffusion, and desorption can be controlled and tailored toward obtaining an ordered, self-assembled DNA origami lattice [23].

Besides the ratio of monovalent and divalent cations, DNA adsorption at solid surfaces is also affected by pH [31, 32], ionic strength [32, 33], DNA conformation [31, 34], and cation species [25, 26, 30, 35]. Therefore, all these factors can be expected to affect the surface mobility of the DNA origami nanostructures and thus the quality of the resulting lattice. In this work, we thus investigated the formation of DNA origami lattices under

Address correspondence to adrian.keller@uni-paderborn.de

the influence of different monovalent and divalent cations, i.e., Li^+, Na^+, K^+, Mg^{2+}, and Ca^{2+}, which were chosen because of their different properties and biological interactions. The formation of DNA origami lattices and the resulting lattice order was monitored *in situ* and in real-time using high-speed atomic force microscopy (HS-AFM). HS-AFM is a powerful and frequently employed tool for visualizing the dynamics of DNA strands and DNA nanostructures [36–40]. Using computer vision algorithms and extracting different topological observables, we found that DNA origami lattice formation, lattice assembly kinetics, and lattice order are strongly affected by the species of the monovalent cations in combination with Mg^{2+}. Moreover, Ca^{2+} combined with Na^+ was found to promote the formation of DNA origami lattices with strongly increased order compared to those assembled with Mg^{2+}. All these effects can be rationalized by the different ion–DNA and ion–mica interactions. As we demonstrate, our results offer a straightforward route toward the fabrication of highly ordered DNA lattices.

2 Experimental

Triangular DNA origami nanostructures were prepared using the 7249-nt long M13mp18 scaffold strand with 208 staple strands (Metabion) in 1× TAE (Carl Roth) containing 10 mM $MgCl_2$ (Sigma–Aldrich) [13]. The mixture was heated rapidly to 80 °C and subsequently cooled to room temperature over 90 min in a Thermocycler Primus 25 advanced (PEQLAB). The assembled structures were purified by spin filtering (Amicon Ultra, 100K, Millipore) in 1× TAE containing 10 mM $MgCl_2$ to remove excess staple strands. The final concentration of the synthesized DNA origami triangles was determined using an Implen Nanophotometer P330.

DNA origami lattice formation and dynamics were monitored by HS-AFM using a JPK Nanowizard ULTRA Speed with USC F0.3-k0.3 cantilevers (NanoWorld). Each measurement was performed in a liquid cell with 2 nM DNA origami triangles in 1× TAE buffer containing 10 mM $MgCl_2$ or $CaCl_2$ (VWR Chemicals) and 75 mM of a monovalent metal salt, that is either NaCl (Sigma-Aldrich), LiCl (Sigma-Aldrich), or KCl (Merck). Images were recorded with 3 μm × 3 μm scan size, 10 Hz line rate, and 512 pixels × 512 pixels resolution, resulting in 51.2 s per frame. The first image of each time series was recorded about 5 min after injection of the DNA origami solution. For the experiment with a higher DNA origami concentration of 3 nM, incubation was also carried out in a liquid cell but without scanning. After 90 min incubation, a single HS-AFM image was recorded.

DNA origami lattice order was quantified by determining the correlation length from the AFM images as previously described [23, 24]. Briefly, the radial power spectral density function was calculated for each HS-AFM image using Gwyddion [41]. This function exhibits a distinct correlation peak at the reciprocal periodicity of the pattern. The full width at half maximum of this peak corresponds to the inverse correlation length ξ. We also made use of the OpenCV library [42] to extract the coordinates of the DNA origami triangles in the images (further details and python and R codes are included in the Electronic Supplementary Material (ESM)). As the correlation length only provides information about distances (isotropically averaged), we quantified lattice order using Delaunay triangulation of the coordinates and computed the nearest-neighbor distribution and related observables (for instance, Lemaitre plots, as a measure of order; see Ref. [43] for details) and the fraction of DNA origami triangles in the largest cluster (as a measure of coverage). Further details are provided in the ESM.

3 Results and discussion

3.1 Influence of monovalent cation species on lattice order

Since Na^+ cations have been shown to be effective in achieving a well-ordered DNA origami lattice with an optimized Na^+/Mg^{2+} ratio of 7.5 [23], we used the same ratio throughout the experiments. We first varied the monovalent cation species, while maintaining Mg^{2+} as the divalent cation. Compared to our previous work, here we used a lower DNA origami concentration (2 nM instead of 3 nM) to slow down monolayer formation and monitor the lattice assembly in more detail. The HS-AFM images and their corresponding two-dimensional (2D) fast Fourier transforms (FFTs) shown in Figs. 1(a)–1(c) make it clear immediately that varying the monovalent cation species results in very different lattice assembly dynamics. In particular, it is rather obvious that monolayer formation proceeds faster in the Na^+-containing system (Fig. 1(b)) than in the presence of the other monovalent cations. In the following discussion, we shall use the established system based on the competition of Na^+ and Mg^{2+} ions as the benchmark for the evaluation of these ion-specific differences.

As can be seen in Fig. 1(b), for the Mg^{2+}/Na^+ system, an ordered monolayer of DNA origami triangles was obtained after incubation for 40 min. The resulting lattice has a well-defined hexagonal symmetry, which is clearly reflected in its corresponding FFT. However, it is worth noting that this hexagonal order is short-ranged as shown in Fig. 2(b), where we depict the corresponding Delaunay triangulation of the lattices obtained for each system in Fig. 2(a). Even though the FFT of the Mg^{2+}/Na^+ lattice in Fig. 2(a) shows 6 well-defined peaks in the central hexagon and several additional higher-order peaks, the corresponding triangulation in Fig. 2(b) does not display a single hexagonal lattice. Rather, several densely populated grains that each display a local hexagonal symmetry can be identified. These grains, however, are separated by less populated areas without discernible order.

As can be seen in Fig. 1(a), replacing Na^+ with Li^+ ions while maintaining the ratio of mono- to divalent ions did not lead to a closed DNA origami monolayer within 40 min of incubation, even though the corresponding FFT develops a weak hexagonal symmetry indicative of at least some degree of hexagonal ordering. A closed DNA origami monolayer was not formed until 60 min of incubation (Fig. 2(a)). In order to quantify DNA origami triangle packing, we show in Fig. 2(c) the correlation lengths ξ of all the lattices obtained for the different systems upon the formation of a closed DNA origami monolayer. As can be seen, the lattice formed in the presence of Li^+ ions had a correlation length that was only 2.4 times the lattice periodicity λ. The Na^+-mediated monolayer, on the other hand, had a correlation length of 3.4λ and thus exhibited much higher packing.

To quantify lattice order, in Fig. 2(d), we present the Lemaitre plot corresponding to the morphologies of the initial lattices shown in Fig. 2(a). The Lemaitre plot is a diagram where the variance of the distribution of nearest neighbors (μ_2) is plotted against the relative proportion of DNA origami triangles with exactly 6 neighbors (p_6). It allows contextualizing order on a scale in which the rightmost point (corresponding to $p_6 = 1$) is an infinite perfect honeycomb and the limit $p_6 \to 0$ is only achievable in extreme cases where the distribution of neighbors is forced to have an artificially large variance. The exact form of the curve is not known analytically but it can be well approximated by the 2 (broken and solid) curves shown in

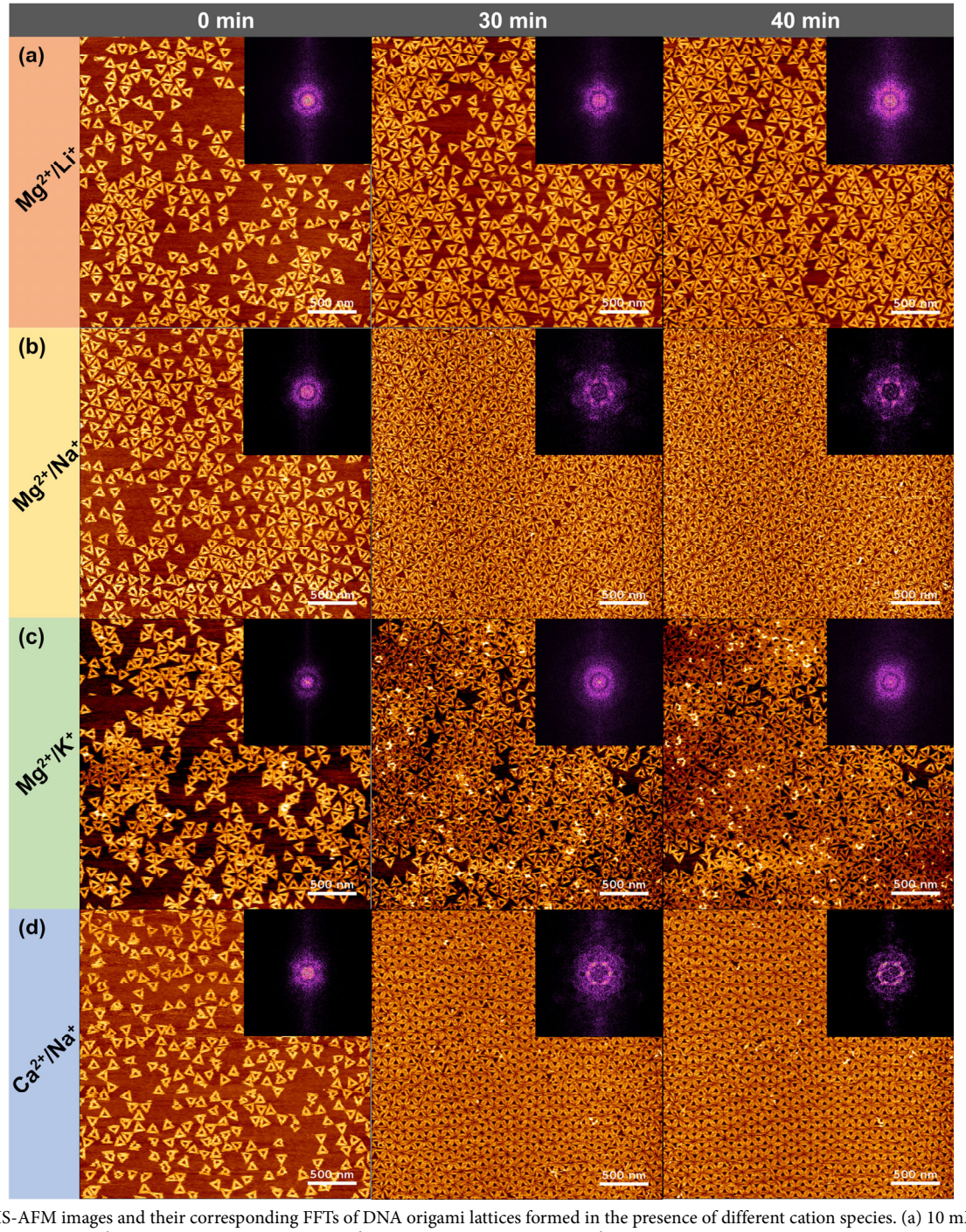

Figure 1 HS-AFM images and their corresponding FFTs of DNA origami lattices formed in the presence of different cation species. (a) 10 mM Mg^{2+} and 75 mM Li^{+}. (b) 10 mM Mg^{2+} and 75 mM Na^{+}. (c) 10 mM Mg^{2+} and 75 mM K^{+}. (d) 10 mM Ca^{2+} and 75 mM Na^{+}. Scale bars are 500 nm.

Fig. 2(d) [44]. For a perfect hexagonal pattern, we have a perfect tessellation made of regular hexagons. In that case the distribution of neighbors is simply $p_6 = 1$. If we reduce the order, then some hexagons are replaced by pentagons (5 neighbors) and heptagons (7 neighbors). To first approximation, we can assume that $p_j = 0$ for $j \neq 5, 6, 7$. In that case, imposing that the mean is still 6, we have a set of simple linear equations

$$p_5 + p_6 + p_7 = 1 \quad (1)$$

$$5p_5 + 6p_6 + 7p_7 = 6 \quad (2)$$

$$(5-6)^2 p_5 + (6-6)^2 p_6 + (7-6)^2 p_7 = \mu_2 \quad (3)$$

where μ_2 is the variance of the distribution of neighbors. The solution of these equations is simply

$$\mu_2 = 1 - p_6 \quad (4)$$

which is remarkably accurate for $p_6 > 0.7$.

On the other hand, if we assume that the center of the triangles is less ordered, then we can assume that the distribution of neighbors follows a normal distribution with mean = 6 and variance μ_2. In that case, the mode of the distribution (p_6) is related to the variance through the expression

$$\mu_2 = (2\pi p_6^2)^{-1}, \text{ if } \quad p_6 < 0.7 \quad (5)$$

In conclusion, those lattices closer to the straight line can be assumed to be formed almost exclusively by pentagons, hexagons, and heptagons. The farther a lattice from this straight line, the more randomly the triangles are distributed. Hence, we use

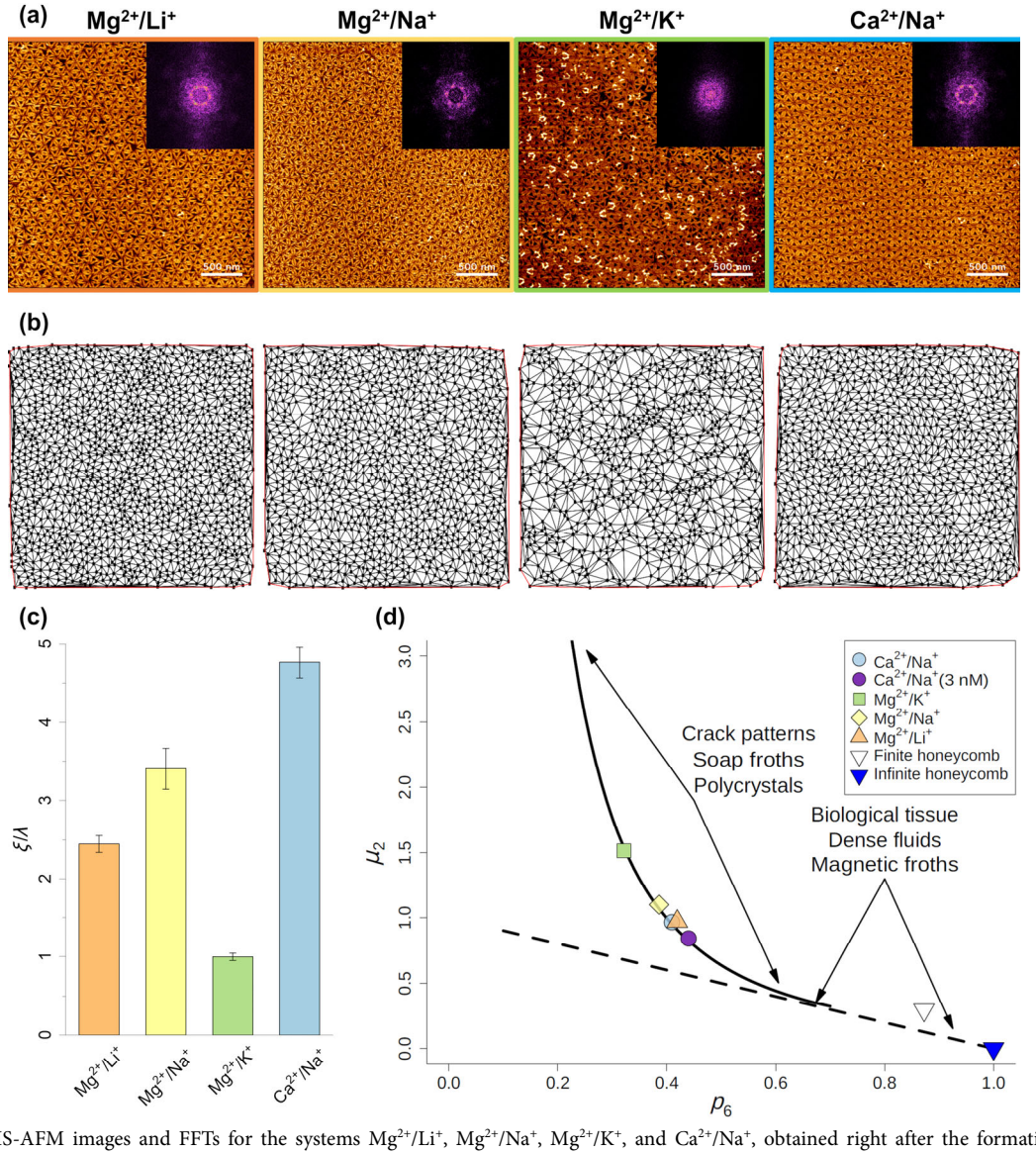

Figure 2 (a) HS-AFM images and FFTs for the systems Mg^{2+}/Li^{+}, Mg^{2+}/Na^{+}, Mg^{2+}/K^{+}, and Ca^{2+}/Na^{+}, obtained right after the formation of a closed monolayer, i.e., after 60, 40, 60, and 30 min, respectively. (b) Corresponding Delaunay triangulation based on the location of the center of the DNA origami triangles in the HS-AFM images in (a). (c) Corresponding relative correlation length ξ/λ of the assembled lattices. (d) The Lemaitre plot: The parameters p_6 and μ_2 represent, respectively, the relative frequency of DNA origami triangles surrounded by exactly 6 nearest neighbors and the variance of the nearest neighbor distribution (see Ref. [43] and ESM for details). The broken and solid curves follow Eqs. (4) and (5), respectively. For comparison, the regions of location of other natural and artificial patterns are indicated in the plot. Those data points closer to the broken line correspond to patterns formed almost exclusively by pentagons, hexagons, and heptagons, whereas those farther from that line are more randomly distributed. The data for a finite and an infinite honeycomb lattice are shown as well. Due to finite-size effects, the finite honeycomb does not fall precisely on the line and has $p_6 < 1$.

the values of μ_2 and p_6 to quantify the order of the triangle arrangement.

Typically, values between $0.4 < p_6 < 0.7$ are considered as intermediate order and $p_6 < 0.4$ as high disorder. For all the lattices shown in Fig. 2, we can assume that the degree of order is intermediate. Interestingly, by inspection of both the correlation length (which quantifies triangle packing alone) and the Lemaitre diagram (which quantifies also the homogeneity in the distribution of the number of nearest neighbors), we can have a richer idea of the differences among the experiments. In particular, in Fig. 2(d), we find that the lattice obtained for the Mg^{2+}/Li^{+} system actually displays a higher degree of order than the corresponding Mg^{2+}/Na^{+} lattice, despite its lower correlation length. This apparent discrepancy can be explained by the fact that the two quantities measure different independent aspects of what we call order. The correlation length is a measure of the average domain size. The Lemaitre plot in Fig. 2(d), on the other hand, characterizes the distribution of the number of nearest neighbors and thus includes ordering both within and between domains. We can, therefore, conclude that the Mg^{2+}/Li^{+} lattice has a smaller average domain size than the Mg^{2+}/Na^{+} lattice while at the same time there is either less disorder within the individual domains or between them.

In sum, these observations suggest that Li^{+} is less efficient than Na^{+} in terms of replacing Mg^{2+} from the mica–DNA interface and thereby promoting the formation of a DNA origami lattice. Since Li^{+} ions interact with the phosphate groups of the DNA backbone in a similar way as Na^{+} [45, 46], this may be attributed to the smaller atomic radius of Li^{+} compared to Na^{+}. The small atomic radius of Li^{+} results in a much higher charge density than for other alkali metal ions, which in turn leads to strongly different hydration behaviors. It is well established that Li^{+} has more pronounced and more tightly bound hydration shells than for example Na^{+} [47–50]. Recently, it was shown that these differences in hydration also result in very different adsorption behaviors [51]. In particular, the authors found

that Li^+ has a much lower probability of penetrating into the first layer of water molecules at a solid surface than other alkali ions and that it is more likely to adsorb in a doubly hydrated form. Therefore, we assume that the Li^+ ions are not able to replace the Mg^{2+} ions from the mica–DNA interface efficiently enough to disrupt a sufficient number of salt bridges to provide the DNA origami triangles with the required lateral mobility to form a high-quality lattice.

We next employed K^+ as the monovalent cation. However, despite having similar hydration properties as Na^+, the results were quite different. As can be seen in Fig. 1(c), DNA origami nanostructures adsorbing on top of each other were observed already in the very beginning of the experiment. With increasing incubation time, this pile-up of DNA origami triangles was getting worse. After 40 min of incubation, a severe build-up of DNA origami multilayers can be seen in Fig. 1(c), even though no closed monolayer has formed yet. The corresponding FFTs show only blurred rings indicating amorphous structures, which is also in agreement with the short correlation length of $\xi = 1.0\lambda$ (see Fig. 2(c)). This exceptionally low ξ value implies that the surface does not show any order at all. This can be attributed to the pile-up of DNA origami triangles, which covers the first incomplete monolayer whose order then cannot be reliably analyzed anymore. Consequently, the lattice obtained for the Mg^{2+}/K^+ system also shows by far the lowest ordering in the Delaunay triangulation and the Lemaitre plot in Figs. 2(b) and 2(d). In Figs. S4 and S5 in the ESM, we show other metrics confirming this observation based on cluster sizes and histograms of the nearest neighbors.

These findings are consistent with recent observations by Sønderskov et al., who found that the Mg^{2+} ions adsorbed at a mica surface can be partially replaced by Na^+ and Li^+ ions, thereby inducing desorption of DNA origami nanostructures. In contrast, in the presence of K^+, the DNA origami nanostructures continued to adsorb at the mica surface, owing to the Mg^{2+} remaining confined at the mica–DNA interface [26]. However, our results also reveal that the addition of K^+ stimulates the build-up of DNA origami multilayers, suggesting that it affects the DNA–DNA interaction and in particular reduces electrostatic repulsion between the negatively charged DNA origami nanostructures. This indicates that the K^+ ions preferentially interact with the DNA and not with the mica surface. In general, Mg^{2+}, Na^+, and Li^+ ions all interact preferentially with the phosphate groups in the DNA backbone, whereas K^+ mostly binds to the nucleobases via the major and the minor grooves [46, 52–54]. This enables the Mg^{2+} ions to remain bound to the phosphate groups, while K^+ additionally binds to the nucleobases, thereby further contributing to the neutralization of the DNA origami nanostructures and thus reducing their electrostatic repulsion. The rapid DNA origami pile-up from the very beginning of the experiment even indicates that the combined binding of Mg^{2+} and K^+ promotes a partial charge inversion of the DNA origami nanostructures and thus leads to attractive electrostatic interactions, as generally observed in DNA condensation by multivalent ions [55–57].

3.2 Influence of divalent cation species on lattice order

In addition to Mg^{2+} ions, various other divalent cations have been shown to be effective in promoting DNA adsorption to mica surfaces, for instance, Ca^{2+}, Zn^{2+}, Ni^{2+}, and Co^{2+} [25, 30, 58, 59]. Given that the transition metal ions, i.e., Zn^{2+}, Ni^{2+}, and Co^{2+}, are able not only to bind strongly to the mica surface but also simultaneously to the DNA backbone phosphates and the nucleobases [25, 60], we do not expect them to be impacted by the addition of monovalent cations. Therefore, in order to investigate the effect of divalent cations on DNA origami lattice formation, Ca^{2+} was chosen to replace Mg^{2+}. Since our results discussed above revealed that Na^+ is the most potent monovalent cation for stimulating the assembly of high-quality DNA origami lattices, we investigated only the combination Ca^{2+}/Na^+. As can be seen in Figs. 1(d) and 3(a), the DNA origami triangles seemed to be blurred and deformed under HS-AFM, before the complete monolayer was formed. This implies that the DNA origami nanostructures underwent rapid diffusive motions on the mica surface. Thanks to this rapid lateral diffusion of the DNA origami triangles on the Ca^{2+}/Na^+-terminated mica surface, a complete monolayer was formed already after 30 min of incubation (see Fig. 1(d)). Despite the shorter incubation time, the formed lattice exhibited a much larger correlation length $\xi = 4.8\lambda$ compared to the value of 3.4λ obtained for the Mg^{2+}/Na^+ system (see Fig. 2(c)). This is evidence that an even higher degree of lattice order can be achieved by using Ca^{2+} instead of Mg^{2+} as the divalent cation.

Since Ca^{2+}/Na^+ appears to be the most promising system for achieving high lattice order, we have followed the evolution of the DNA origami lattices in more detail. Figures 3(a) and 3(b) show 3 HS-AFM images obtained after 10, 60, and 90 min of lattice assembly and the corresponding Delaunay triangulation. At first glance, the lattice does not appear to undergo any significant rearrangements between 60 and 90 min of incubation. This is somewhat reflected also in Fig. 3(c), which plots the calculated correlation length of the Ca^{2+}/Na^+ lattice as a function of incubation time. Here, a sudden increase in the correlation length is observed between 20 and 30 min of incubation. Computing the fraction of DNA origami triangles in the largest cluster (defined as a set of DNA origami triangles with at least another DNA origami triangle at distance λ) we find that this sudden increase was correlated with full surface coverage, which occurred abruptly at around the same time (see Fig. 3(d)). Naturally, for longer incubation times, the fraction of DNA origami triangles in the largest cluster saturated as this cluster spanned the whole surface area observed in the HS-AFM image. Figure 3(e) tracks the evolution of the lattice for different incubation times by plotting the 2 moments μ_2 and p_6 independently as a function of time (see Fig. S3 in the ESM for the corresponding Lemaitre plot). In the first 30 min of incubation, μ_2 becomes smaller and eventually saturates, as a closed monolayer is obtained. As expected from Eq. (5), an inverse yet less pronounced trend is observed for p_6. However, as can be seen in Fig. 3(c), the correlation length did not saturate immediately upon the formation of a closed DNA origami monolayer at about 30 min but rather displayed some fluctuations and also a slight increase for even longer incubation times. After 90 min of incubation, a correlation length of $\xi/\lambda = 5.5 \pm 0.2$ was obtained, compared the value of $\xi/\lambda = 4.8 \pm 0.2$ of the initial lattice formed after 30 min. This indicates that even after the formation of a closed monolayer, there was still some dynamics in the lattice which might have lead to the annealing of some of the remaining lattice defects, as observed previously for the Mg^{2+}/Na^+ system [23].

The more rapid assembly of the DNA origami lattice and the increased lattice order in the presence of Ca^{2+} compared to Mg^{2+} can be attributed to the differences in their interaction with nucleic acids. In particular, Ca^{2+} has a lower affinity for binding to the backbone phosphates than Mg^{2+}, which, however, is still much higher than the affinity of Na^+ ions [54, 61, 62]. At the 7.5-fold excess of Na^+, it is thus easier for the Na^+ ions to replace the Ca^{2+} than the Mg^{2+} salt bridges. Hence, the attractive interactions between the DNA origami nanostructures and

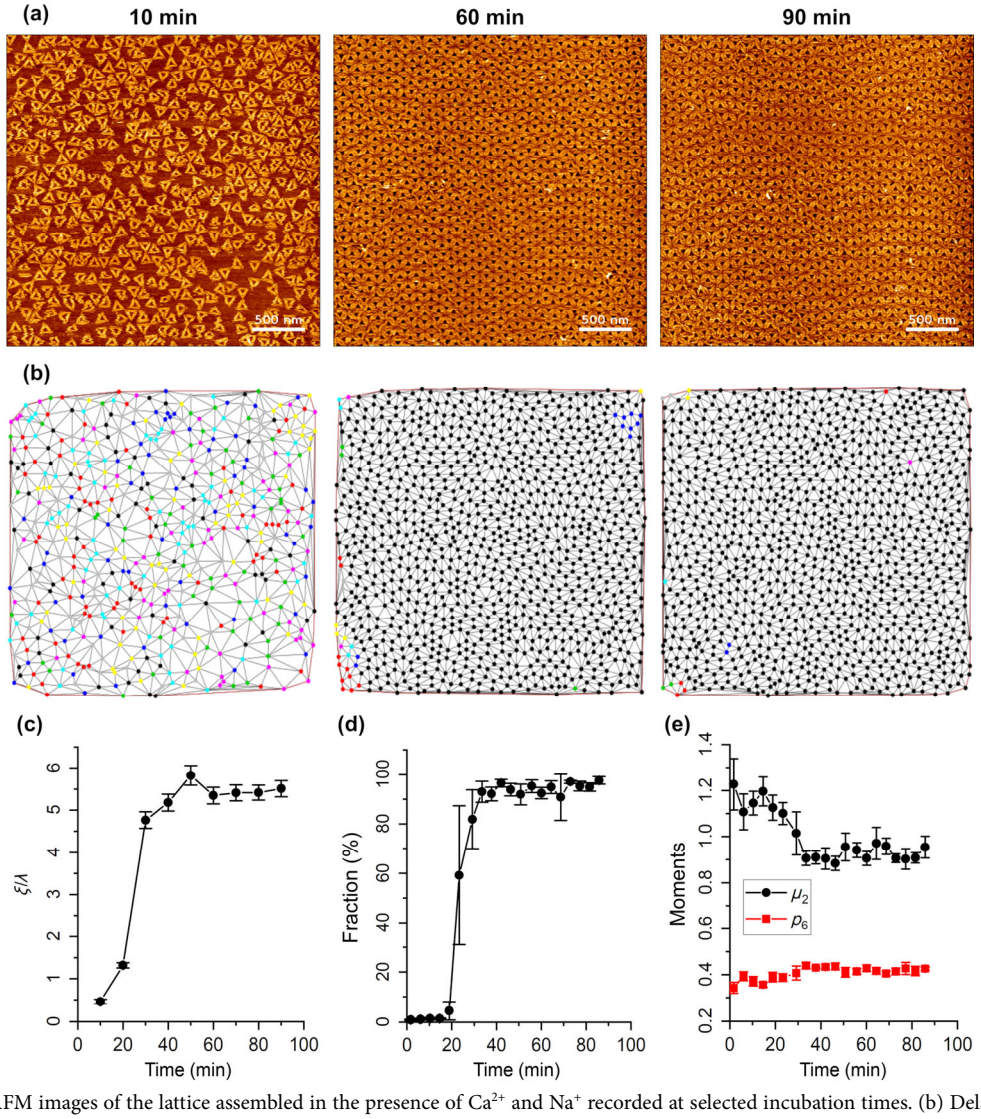

Figure 3 (a) HS-AFM images of the lattice assembled in the presence of Ca^{2+} and Na^{+} recorded at selected incubation times. (b) Delaunay triangulation of the morphologies in (a). Different clusters are shown in different colors. Note how, for long times, almost all the triangles are clustered together. (c) Relative correlation length ξ/λ of the DNA origami lattice as a function of incubation time. (d) Fraction of DNA origami triangles in the largest connected cluster as a function of incubation time. (e) Moments μ_2 and p_6 of the DNA origami lattice as a function of incubation time. The data points in (d) and (e) are averaged over five-minute windows.

the mica surface are weakened in the Ca^{2+}/Na^{+} system, which results in slightly enhanced diffusion of the DNA origami triangles on the mica surface. Enhanced surface diffusion, in turn, allows the adsorbed DNA origami triangles to find their optimum binding site more quickly so that full surface coverage is achieved in a shorter time. Furthermore, enhanced surface mobility of the DNA origami triangles allows them to rearrange more easily after incorporation into the lattice, which enables them to anneal lattice defects more efficiently [23]. This then leads to a better-ordered lattice.

The maximum correlation length obtained for the optimized conditions of 10 mM Ca^{2+}, 75 mM Na^{+}, and 90 min incubation is about 5.5λ (see Fig. 3(c)). This value is comparable to the one we previously observed for 10 mM Mg^{2+}, 75 mM Na^{+}, and ~ 40 min incubation and to correlation lengths routinely observed for other self-organized isotropic patterns [23]. However, in our previous experiments, we used a higher DNA origami concentration of 3 nM, which indicates that also the DNA origami concentration plays a role in the development of lattice order. Assuming the same increase in the correlation length upon switching from Mg^{2+} to Ca^{2+} and prolonging the incubation time to 90 min, it should thus be possible to obtain a highly ordered lattice with a correlation length > 8λ. To test this hypothesis, we have performed one more experiment using the Ca^{2+}/Na^{+} system with a higher DNA origami concentration of 3 nM. The lattice obtained after 90 min of incubation is shown in Fig. 4 together with the corresponding FFT and the Delaunay triangulation. Indeed, the lattice assembled under these conditions showed an exceptionally high degree of order. In perfect agreement with the above prediction, this particular lattice exhibited a correlation length of ξ = 8.2λ, which is by far the largest correlation length we ever obtained in our experiments. Also, in Fig. 2(d), we show that the Lemaitre plot confirms that this is, indeed, the most ordered sample (the purple dot is the rightmost of all the experiments). Furthermore, this experiment demonstrates that the individual parameters ion species, DNA origami concentration, and incubation time are indeed independent. These parameters can thus be adjusted independently to obtain a lattice with the desired order.

4 Conclusions

In summary, we have investigated the formation of ordered lattices of DNA origami triangles on the mica surface under

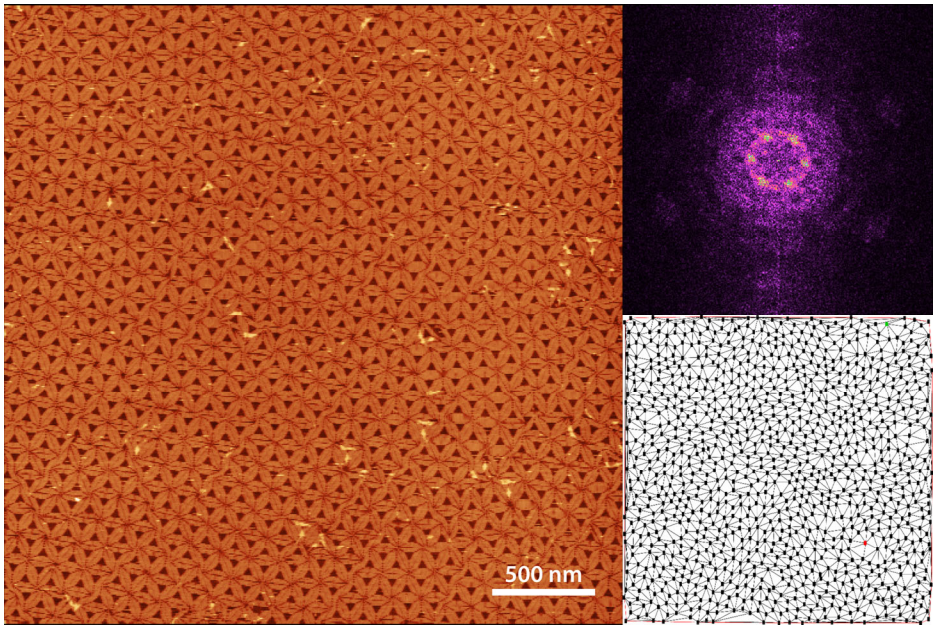

Figure 4 HS-AFM image as well as corresponding FFT and Delaunay triangulation of the assembled lattice obtained for the system Ca^{2+}/Na^{+} with 3 nM DNA origami triangles after incubation for 90 min.

the influence of different monovalent and divalent cations at a molar excess of 7.5 to 1. Under these conditions, the negatively charged DNA origami nanostructures are adsorbed to the negatively charged mica surface via salt bridges formed by the divalent cations. The role of the monovalent cations is to replace some of the divalent ions, disrupt a number of salt bridges, and thereby weaken the electrostatic attraction between the DNA origami nanostructures and the mica surface. This then results in increased surface mobility of the adsorbed DNA origami nanostructures, which facilitates the assembly of an ordered DNA origami lattice. Since different cations interact differently with DNA as well as with the mica surface, they have distinct effects on the development of the lattice and the resulting order.

Our results clearly show that Na^{+} is the most potent of the monovalent ions in partially disrupting the Mg^{2+} salt bridges at the mica–DNA interface. Therefore, Na^{+} facilitates the formation of highly regular DNA origami lattices. Li^{+}, on the other hand, is less effective in promoting lattice assembly. In particular, it takes longer to form a closed DNA origami monolayer in the presence of Li^{+} than for Na^{+} and the resulting lattice has lower quality. This can be attributed to the fact that Li^{+} is a strongly hydrated ion with tightly bound hydration shells that does neither adsorb as strongly to surfaces nor bind as tightly to the phosphates in the DNA backbone as other alkali ions. It therefore does not disrupt the Mg^{2+} salt bridges at the mica–DNA interface as efficiently.

K^{+} is often considered rather similar to Na^{+} in its binding and adsorption behavior. Nonetheless, in the presence of K^{+}, disordered DNA origami multilayers instead of ordered monolayer lattices are formed on the mica surface. This is a direct result of the different DNA-binding modes of both ions. While Na^{+} competes with Mg^{2+} for the same binding sites in the DNA backbone, K^{+} binds preferentially to the nucleobases. The different binding modes of these two alkali cations have previously been found to affect also DNA origami stability under low-Mg^{2+} conditions [27]. In the present experiments at high Mg^{2+} concentrations, the additional K^{+} binding to the DNA origami nanostructures rather results in DNA neutralization and promotes charge inversion by the phosphate-bound Mg^{2+} ions. This leads to DNA origami condensation and the subsequent pile-up of multilayers already at very short incubation times.

When it comes to the divalent cations, we found that Ca^{2+} combined with Na^{+} promotes the formation of DNA origami monolayers with higher order and at shorter incubation times than the Mg^{2+}/Na^{+} system. This is due to the weaker interaction of Ca^{2+} both with the mica surface and the DNA's backbone phosphates, which allows the Ca^{2+} salt bridges to be disrupted more easily by Na^{+} than the alternative Mg^{2+} salt bridges. When a closed DNA origami monolayer is formed, the Ca^{2+}/Na^{+} system thus displays a correlation length of 4.8λ that is about 40% larger than that of the corresponding Mg^{2+}/Na^{+} lattice. This increase in lattice quality is also reflected in the other topological observables. Finally, also the DNA origami concentration is found to have an effect on lattice quality and order. By independently optimizing these factors, i.e., cation species, DNA origami concentration, and assembly time, we obtain a highly ordered DNA origami lattice with an unprecedented correlation length of $\xi = 8.2\lambda$.

Our results demonstrate that a simple exchange of $MgCl_2$ for $CaCl_2$ enables a drastic increase in lattice order. Therefore, exploiting ion-specific interactions to control DNA origami surface mobility provides an easy means for obtaining highly ordered DNA origami lattices on mica surfaces. For many applications in molecular lithography and surface engineering [5, 63], however, other substrate materials such as silicon or glass are more desirable. Unfortunately, the cation-related effects observed in this work are very specific to mica surfaces and cannot be directly transferred to other surfaces. Nevertheless, mica surfaces may be used as templates to grow highly-ordered DNA origami lattices, which subsequently could be cross-linked for instance by sticky-end hybridization [19], desorbed from the template surface in high Na^{+} concentrations [18], and possibly transferred to another, more relevant substrate surface. This templating and transfer-based approach would be similar to the one routinely employed in the production of large-area single-crystalline graphene sheets [64], and have the great advantage of being independent of the target substrate. While in this work, we were able to optimize the first step of this general approach, future studies are required to validate and optimize also the other steps.

Acknowledgements

We thank David Contreras for his helpful discussions and comments. This research has been partially funded by the Spanish Ministerio de Ciencia, Innovacion y Universidades-FEDER funds of the European Union support, under projects FIS2016-78883-C2-2-P and PID2019-106339GB-I00 (M.C.).

Funding note: Open access funding provided by Projekt DEAL.

Electronic Supplementary Material: Supplementary material (automatic topological analysis, code listings, additional plots, HS-AFM movies) is available in the online version of this article at https://doi.org/10.1007/s12274-020-2985-4.

References

[1] Cheng, W.; Rechberger, F.; Niederberger, M. From 1D to 3D—macroscopic nanowire aerogel monoliths. *Nanoscale* **2016**, *8*, 14074–14077.

[2] Sundrani, D.; Darling, S. B.; Sibener, S. J. Guiding polymers to perfection: Macroscopic alignment of Nanoscale domains. *Nano Lett*. **2004**, *4*, 273–276.

[3] Aizenberg, J.; Weaver, J. C.; Thanawala, M. S.; Sundar, V. C.; Morse, D. E.; Fratzl, P. Skeleton of *Euplectella* sp.: Structural hierarchy from the Nanoscale to the Macroscale. *Science* **2005**, *309*, 275–278.

[4] Liu, L. Q.; Ma, W. J.; Zhang, Z. Macroscopic carbon nanotube assemblies: Preparation, properties, and potential applications. *Small* **2011**, *7*, 1504–1520.

[5] Hui, L. W.; Zhang, Q. M.; Deng, W.; Liu, H. T. DNA-based nanofabrication: Pathway to applications in surface engineering. *Small* **2019**, *15*, 1805428.

[6] Seeman, N. C. DNA in a material world. *Nature* **2003**, *421*, 427–431.

[7] Aryal, B. R.; Ranasinghe, D. R.; Westover, T. R.; Calvopiña, D. G.; Davis, R. C.; Harb, J. N.; Woolley, A. T. DNA origami mediated electrically connected metal–semiconductor junctions. *Nano Res*. **2020**, *13*, 1419–1426.

[8] Teschome, B.; Facsko, S.; Schönherr, T.; Kerbusch, J.; Keller, A.; Erbe, A. Temperature-dependent charge transport through individually contacted DNA origami-based Au nanowires. *Langmuir* **2016**, *32*, 10159–10165.

[9] Masciotti, V.; Piantanida, L.; Naumenko, D.; Amenitsch, H.; Fanetti, M.; Valant, M.; Lei, D. S.; Ren, G.; Lazzarino, M. A DNA origami plasmonic sensor with environment-independent read-out. *Nano Res*. **2019**, *12*, 2900–2907.

[10] Tapio, K.; Leppiniemi, J.; Shen, B. X.; Hytönen, V. P.; Fritzsche, W.; Toppari, J. J. Toward single electron nanoelectronics using self-assembled DNA structure. *Nano Lett*. **2016**, *16*, 6780–6786.

[11] Choi, Y.; Kotthoff, L.; Olejko, L.; Resch-Genger, U.; Bald, I. DNA origami-based Förster resonance energy-transfer nanoarrays and their application as ratiometric sensors. *ACS Appl. Mater. Interfaces* **2018**, *10*, 23295–23302.

[12] Koo, K. M.; Carrascosa, L. G.; Trau, M. DNA-directed assembly of copper nanoblocks with inbuilt fluorescent and electrochemical properties: Application in simultaneous amplification-free analysis of multiple RNA species. *Nano Res*. **2018**, *11*, 940–952.

[13] Rothemund, P. W. K. Folding DNA to create nanoscale shapes and patterns. *Nature* **2006**, *440*, 297–302.

[14] Douglas, S. M.; Dietz, H.; Liedl, T.; Högberg, B.; Graf, F.; Shih, W. M. Self-assembly of DNA into nanoscale three-dimensional shapes. *Nature* **2009**, *459*, 414–418.

[15] Dietz, H.; Douglas, S. M.; Shih, W. M. Folding DNA into twisted and curved nanoscale shapes. *Science* **2009**, *325*, 725–730.

[16] Andersen, E. S.; Dong, M. D.; Nielsen, M. M.; Jahn, K.; Subramani, R.; Mamdouh, W.; Golas, M. M.; Sander, B.; Stark, H.; Oliveira, C. L. P. et al. Self-assembly of a nanoscale DNA box with a controllable lid. *Nature* **2009**, *459*, 73–76.

[17] Suzuki, Y.; Sugiyama, H.; Endo, M. Complexing DNA origami frameworks through sequential self-assembly based on directed docking. *Angew. Chem., Int. Ed*. **2018**, *57*, 7061–7065.

[18] Ramakrishnan, S.; Subramaniam, S.; Stewart, A. F.; Grundmeier, G.; Keller, A. Regular Nanoscale protein patterns via directed adsorption through self-assembled DNA origami masks. *ACS Appl. Mater. Interfaces* **2016**, *8*, 31239–31247.

[19] Kocabey, S.; Kempter, S.; List, J.; Xing, Y. Z.; Bae, W.; Schiffels, D.; Shih, W. M.; Simmel, F. C.; Liedl, T. Membrane-assisted growth of DNA origami nanostructure arrays. *ACS Nano* **2015**, *9*, 3530–3539.

[20] Woo, S.; Rothemund, P. W. K. Self-assembly of two-dimensional DNA origami lattices using cation-controlled surface diffusion. *Nat. Commun*. **2014**, *5*, 4889.

[21] Rafat, A. A.; Pirzer, T.; Scheible, M. B.; Kostina, A.; Simmel, F. C. Surface-assisted large-scale ordering of DNA origami tiles. *Angew. Chem., Int. Ed*. **2014**, *53*, 7665–7668.

[22] Suzuki, Y.; Endo, M.; Sugiyama, H. Lipid-bilayer-assisted two-dimensional self-assembly of DNA origami nanostructures. *Nat. Commun*. **2015**, *6*, 8052.

[23] Kielar, C.; Ramakrishnan, S.; Fricke, S.; Grundmeier, G.; Keller, A. Dynamics of DNA origami lattice formation at solid–liquid interfaces. *ACS Appl. Mater. Interfaces* **2018**, *10*, 44844–44853.

[24] Xin, Y.; Ji, X. Y.; Grundmeier, G.; Keller, A. Dynamics of lattice defects in mixed DNA origami monolayers. *Nanoscale* **2020**, *12*, 9733–9743.

[25] Pastré, D.; Piétrement, O.; Fusil, S.; Landousy, F.; Jeusset, J.; David, M. O.; Hamon, L.; Le Cam, E.; Zozime, A. Adsorption of DNA to mica mediated by divalent Counterions: A theoretical and experimental study. *Biophys. J*. **2003**, *85*, 2507–2518.

[26] Sønderskov, S. M.; Klausen, L. H.; Skaanvik, S. A.; Han, X. J.; Dong, M. D. *In situ* surface charge density visualization of self-assembled DNA nanostructures after ion exchange. *ChemPhysChem* **2020**, *21*, 1474–1482.

[27] Kielar, C.; Xin, Y.; Shen, B. X.; Kostiainen, M. A.; Grundmeier, G.; Linko, V.; Keller, A. On the stability of DNA origami nanostructures in low-magnesium buffers. *Angew. Chem., Int. Ed*. **2018**, *57*, 9470–9474.

[28] Ellis, J. S.; Abdelhady, H. G.; Allen, S.; Davies, M. C.; Roberts, C. J.; Tendler, S. J. B.; Williams, P. M. Direct atomic force microscopy observations of monovalent ion induced binding of DNA to mica. *J. Microsc*. **2004**, *215*, 297–301.

[29] Bezanilla, M.; Manne, S.; Laney, D. E.; Lyubchenko, Y. L.; Hansma, H. G. Adsorption of DNA to mica, silylated mica, and minerals: Characterization by atomic force microscopy. *Langmuir* **1995**, *11*, 655–659.

[30] Kan, Y. J.; Tan, Q. Y.; Wu, G. S.; Si, W.; Chen, Y. F. Study of DNA adsorption on mica surfaces using a surface force apparatus. *Sci. Rep*. **2015**, *5*, 8442.

[31] Romanowski, G.; Lorenz, M. G.; Wackernagel, W. Adsorption of plasmid DNA to mineral surfaces and protection against DNase I. *Appl. Environ. Microbiol*. **1991**, *57*, 1057–1061.

[32] Vandeventer, P. E.; Lin, J. S.; Zwang, T. J.; Nadim, A.; Johal, M. S.; Niemz, A. Multiphasic DNA adsorption to silica surfaces under varying buffer, pH, and ionic strength conditions. *J. Phys. Chem. B* **2012**, *116*, 5661–5670.

[33] Pastré, D.; Hamon, L.; Landousy, F.; Sorel, I.; David, M. O.; Zozime, A.; Le Cam, E.; Piétrement, O. Anionic polyelectrolyte adsorption on mica mediated by multivalent cations: A solution to DNA imaging

by atomic force microscopy under high ionic strengths. *Langmuir* **2006**, *22*, 6651–6660.
[34] Song, Y. H.; Li, Z.; Liu, Z. G.; Wei, G.; Wang, L.; Sun, L. L.; Guo, C. L.; Sun, Y. J.; Yang, T. A novel strategy to construct a flat-lying DNA monolayer on a mica surface. *J. Phys. Chem. B* **2006**, *110*, 10792–10798.
[35] Hansma, H. G.; Laney, D. E. DNA binding to mica correlates with cationic radius: Assay by atomic force microscopy. *Biophys. J.* **1996**, *70*, 1933–1939.
[36] Jiang, Z. X.; Zhang, S.; Yang, C. X.; Kjems, J.; Huang, Y. D.; Besenbacher, F.; Dong, M. D. Serum-induced degradation of 3D DNA box origami observed with high-speed atomic force microscopy. *Nano Res.* **2015**, *8*, 2170–2178.
[37] Lee, A. J.; Szymonik, M.; Hobbs, J. K.; Wälti, C. Tuning the translational freedom of DNA for high speed AFM. *Nano Res.* **2015**, *8*, 1811–1821.
[38] Shiomi, T.; Tan, M. M.; Takahashi, N.; Endo, M.; Emura, T.; Hidaka, K.; Sugiyama, H.; Takahashi, Y.; Takakura, Y.; Nishikawa, M. Atomic force microscopy analysis of orientation and bending of oligodeoxynucleotides in polypod-like structured DNA. *Nano Res.* **2015**, *8*, 3764–3771.
[39] Kielar, C.; Zhu, S. Q.; Grundmeier, G.; Keller, A. Quantitative assessment of tip effects in single-molecule high-speed atomic force microscopy using DNA origami substrates. *Angew. Chem., Int. Ed.* **2020**, in press, DOI: 10.1002/ange.202005884.
[40] Ramakrishnan, S.; Shen, B. X.; Kostiainen, M. A.; Grundmeier, G.; Keller, A.; Linko, V. Real-time observation of superstructure-dependent DNA origami digestion by DNase I using high-speed atomic force microscopy. *ChemBioChem* **2019**, *20*, 2818–2823.
[41] Nečas, D.; Klapetek, P. Gwyddion: An open-source software for SPM data analysis. *Open Phys.* **2012**, *10*, 181–188.
[42] Bradski, G. R.; Kaehler, A. *Learning OpenCV: Computer Vision in C++ with the OpenCV Library*; O'Reilly Media, Inc.: Sebastopol, USA, 2013.
[43] Castro, M.; Cuerno, R.; García-Hernández, M. M.; Vázquez, L. Pattern-wavelength coarsening from topological dynamics in silicon nanofoams. *Phys. Rev. Lett.* **2014**, *112*, 094103.
[44] Le Caer, G. Topological models of 2D cellular structure. *J. Phys. A: Math. Gen.* **1991**, *24*, 4655–4675.
[45] Shen, X.; Gu, B.; Che, S. A.; Zhang, F. S. Solvent effects on the conformation of DNA dodecamer segment: A simulation study. *J. Chem. Phys.* **2011**, *135*, 034509.
[46] Auffinger, P.; D'Ascenzo, L.; Ennifar, E. Sodium and potassium interactions with nucleic acids. In *The Alkali Metal Ions: Their Role for Life*. Sigel, A.; Sigel, H.; Sigel, R. K. O., Eds.; Springer: Cham, 2016; pp 167–201.
[47] Jákli, G. The H_2O–D_2O solvent isotope effects on the molar volumes of alkali-chloride solutions at T = (288.15, 298.15, and 308.15)K. *J. Chem. Thermodyn.* **2007**, *39*, 1589–1600.
[48] Cieplak, P.; Kollman, P. Monte Carlo simulation of aqueous solutions of Li^+ and Na^+ using many-body potentials. Coordination numbers, ion solvation enthalpies, and the relative free energy of solvation. *J. Chem. Phys.* **1990**, *92*, 6761–6767.
[49] Hermansson, K.; Wojcik, M. Water Exchange around Li^+ and Na^+ in LiCl(aq) and NaCl(aq) from MD simulations. *J. Phys. Chem. B* **1998**, *102*, 6089–6097.
[50] Mähler, J.; Persson, I. A study of the hydration of the alkali metal ions in aqueous solution. *Inorg. Chem.* **2012**, *51*, 425–438.
[51] Kiyohara, K.; Minami, R. Hydration and dehydration of monovalent cations near an electrode surface. *J. Chem. Phys.* **2018**, *149*, 014705.
[52] Cheng, Y. H.; Korolev, N.; Nordenskiöld, L. Similarities and differences in interaction of K^+ and Na^+ with condensed ordered DNA. A molecular dynamics computer simulation study. *Nucleic Acids Res.* **2006**, *34*, 686–696.
[53] Pasi, M.; Maddocks, J. H.; Lavery, R. Analyzing ion distributions around DNA: Sequence-dependence of potassium ion distributions from microsecond molecular dynamics. *Nucleic Acids Res.* **2015**, *43*, 2412–2423.
[54] Cruz-León, S.; Schwierz, N. Hofmeister series for metal-cation-RNA interactions: The interplay of binding affinity and exchange kinetics. *Langmuir* **2020**, *36*, 5979–5989.
[55] Besteman, K.; Van Eijk, K.; Lemay, S. G. Charge inversion accompanies DNA condensation by multivalent ions. *Nat. Phys.* **2007**, *3*, 641–644.
[56] Bloomfield, V. A. DNA condensation by multivalent cations. *Biopolymers* **1997**, *44*, 269–282.
[57] Opherden, L.; Oertel, J.; Barkleit, A.; Fahmy, K.; Keller, A. Paramagnetic decoration of DNA origami nanostructures by Eu^{3+} coordination. *Langmuir* **2014**, *30*, 8152–8159.
[58] Thomson, N. H.; Kasas, S.; Smith; Hansma, H. G.; Hansma, P. K. Reversible binding of DNA to mica for AFM imaging. *Langmuir* **1996**, *12*, 5905–5908.
[59] Piétrement, O.; Pastré, D.; Fusil, S.; Jeusset, J.; David, M. O.; Landousy, F.; Hamon, L.; Zozime, A.; Le Cam, E. Reversible binding of DNA on $NiCl_2$-treated mica by varying the ionic strength. *Langmuir* **2003**, *19*, 2536–2539.
[60] Duguid, J.; Bloomfield, V. A.; Benevides, J.; Thomas, G. J. Jr. Raman spectroscopy of DNA-metal complexes. I. Interactions and conformational effects of the divalent cations: Mg, Ca, Sr, Ba, Mn, Co, Ni, Cu, Pd, and Cd. *Biophys. J.* **1993**, *65*, 1916–1928.
[61] Kolev, S. K.; Petkov, P. S.; Rangelov, M. A.; Trifonov, D. V.; Milenov, T. I.; Vayssilov, G. N. Interaction of Na^+, K^+, Mg^{2+} and Ca^{2+} counter cations with RNA. *Metallomics* **2018**, *10*, 659–678.
[62] Petrov, A. S.; Bowman, J. C.; Harvey, S. C.; Williams, L. D. Bidentate RNA–magnesium clamps: On the origin of the special role of magnesium in RNA folding. *RNA* **2011**, *17*, 291–297.
[63] Wang, R. R.; Zhang, G. M.; Liu, H. T. DNA-templated nanofabrication. *Curr. Opin. Colloid Interface Sci.* **2018**, *38*, 88–99.
[64] Gao, L. B.; Ren, W. C.; Xu, H. L.; Jin, L.; Wang, Z. X.; Ma, T.; Ma, L. P.; Zhang, Z. Y.; Fu, Q.; Peng, L. M. et al. Repeated growth and bubbling transfer of graphene with millimetre-size single-crystal grains using platinum. *Nat. Commun.* **2012**, *3*, 699.